

## Article

# The Effect of Infrared Laser Irradiation on the Surface Morphology and Electrical Properties of Zinc Metal

Muhammad Asif <sup>1,2,†</sup>, Anwar Latif <sup>1,\*,†</sup>, Ahsan Ali <sup>3,†</sup>, Muhammad Shahid Rafique <sup>1</sup>, Shakeel Ahmad Khan <sup>4</sup> , Abdul Haseeb <sup>5</sup> and Muhammad Kashif Shahid <sup>6,\*</sup> 

<sup>1</sup> Department of Physics, University of Engineering and Technology, Lahore 54890, Pakistan

<sup>2</sup> Institute of Physics, The Islamia University of Bahawalpur, Bahawalpur 63100, Pakistan

<sup>3</sup> School of Mechanical Engineering, University of Leeds, Leeds LS2 9JT, UK

<sup>4</sup> Department of Applied Biology and Chemical Technology, The Hong Kong Polytechnic University, Hung Hom, Kowloon 999077, Hong Kong

<sup>5</sup> Department of Physics, University of Gothenburg, 41756 Gothenburg, Sweden

<sup>6</sup> Research Institute of Environment & Biosystem, Chungnam National University, Daejeon 34134, Republic of Korea

\* Correspondence: anwarlatif@uet.edu.pk (A.L.); mkbutt2000@gmail.com (M.K.S.)

† These authors contributed equally to this work.

**Abstract:** This study details the irradiation of pure (99.995%) and immaculate metallic Zinc using Nd: YAG laser (1064 nm, 10 mJ, 9–14 ns). The influence and impact of multiple laser shots on the formation of microstructures and crystal structure orientations is assessed. Arrays of ablated craters are machined on the whole surface of the target to probe the electrical and topographical characteristics of laser-treated surfaces. Irradiated samples are examined by multiple characterizing techniques such as scanning electron microscopy (SEM), atomic force microscopy (AFM), X-ray diffraction (XRD), and a four-point probe for electrical conductivity measurements. SEM and AFM analysis exhibited the formation of laser-induced ripple structures with periodicity sheerly dependent on laser shots. A comparison of surface topography of the virgin and treated samples disclosed a pronounced modification in surface texture. The XRD patterns of laser shined targets indicate no momentous structural change in the crystal structure, whereas the measurements on the electrical conductivity of the irradiated surfaces exhibit an exponential descending trend with an augmentation in laser shots.

**Keywords:** electrical conductivity; laser irradiation; microstructures; surface morphology; surface topography



**Citation:** Asif, M.; Latif, A.; Ali, A.; Rafique, M.S.; Khan, S.A.; Haseeb, A.; Shahid, M.K. The Effect of Infrared Laser Irradiation on the Surface Morphology and Electrical Properties of Zinc Metal. *Physchem* **2023**, *3*, 22–33. <https://doi.org/10.3390/physchem3010003>

Academic Editor:  
Michael EG Lyons

Received: 21 October 2022  
Revised: 25 November 2022  
Accepted: 27 December 2022  
Published: 31 December 2022



**Copyright:** © 2022 by the authors. Licensee MDPI, Basel, Switzerland. This article is an open access article distributed under the terms and conditions of the Creative Commons Attribution (CC BY) license (<https://creativecommons.org/licenses/by/4.0/>).

## 1. Introduction

In the last few decades, owing to the advances in engineering and technology, the practical application of radiation technologies has escalated widely in different sectors including material science, nanotechnology, instrumentation, medicine, environmental remediation, energy devices, food industry, etc. [1–4]. Laser irradiation of solids has become an unprecedented and novel tool for material processing and has been extensively studied in the last several decades [5,6]. Laser ablation of materials is a subject of current research on account of its widespread and far-reaching applications in the domain of material processing, industry, micromachining, nano-structuring, laser welding, and cutting, as well as in paint stripping, etching, and surface cleaning [7–10]. Over and above, the laser has emerged as a promising and propitious technology in compound formation [11], metallurgy [12], scribing and shaping of materials along with electronic and semiconductor device fabrication [13,14], optoelectronics [15], sensor [16], pulsed laser deposition [17], etc. Laser irradiation not only changes the thermal, optical, and electrical properties of the metals but also induce defects and variations in grain sizes [18]. Moreover, the interaction

of short laser pulses with solids is accompanied by various instabilities, which may lead to surface modifications, and alteration in electrical and optical properties [19,20].

Studies have reported that the irradiation of material by short laser pulses of fluence close to the ablation threshold, leads to the formation of periodic structures in the form of ripples, ridges, whiskers, and granular structures on the surface [21,22]. As some of these structures are periodic, they are called Laser-induced Periodic Surface Structures (LIPSSs) [23,24]. It is of great significance for the material scientists and surface engineering technology to understand the link between the microstructures and laser processing of materials. Several theories based on the interference of two waves, the incident and surface refracted waves, have been used to expound the mechanisms of the formation of coarse and fine laser-induced periodic surface structures. The surface wave may be diffracted by the microscopic asperities of the irradiated surface by the laser-induced plasma or by surface plasmons and polaritons [25,26].

Zinc is the 4th most commonly worldwide applied metal after iron, aluminum, and copper [27,28]. Zinc is extensively used in oil dwelling fields for anti-corrosion resistance coating and energy storage devices electrodes. The major objective of this study is the evolution and development of the surface morphology, surface topography, structural variations, and electrical conductivity measurements of the metallic zinc targets after exposure to repetitive Nd: YAG laser pulses ranging from 10 to 40. The low pulse range is deliberately selected to investigate the IR radiation impact on zinc metal surficial layer topography/morphology near ablation threshold energy values. Machining of micro pattern is observed only near ablation threshold values. The work holds its novelty in establishment of regular wavy pattern near ablation threshold values. To our knowledge, such grid machine targets have never been studied before (in air) in this range of pulses. The outcomes of this study are concluded based on the empirical and rationalized results obtained from atomic force microscopy (AFM), X-ray diffraction (XRD), scanning electron microscope (SEM), and four-point probe measurement.

## 2. Materials and Methods

### 2.1. Experimental Conditions

Finely polished and well-prepared specimens of pure zinc (99.995%) metal are subjected to IR irradiation with the assistance of Nd: YAG laser having a Gaussian intensity profile. The size of experimentally calculated laser spot on a transparent sheet of polyethyleneterephthalate (PET) (with a single laser shot at a focusing distance of 10 cm), is found to be 50  $\mu\text{m}$  with a laser fluence of 128  $\text{J}/\text{cm}^2$ . Exposure of the test specimens (2 cm  $\times$  1 cm  $\times$  0.1 cm) to laser pulses at  $0^\circ$  angle with the normal to the surface is conducted in ambient air. An IR lens of focal length 10 cm is used to convene the laser pulses tightly on the target. A schematic of experimental setup is presented in Figure 1.

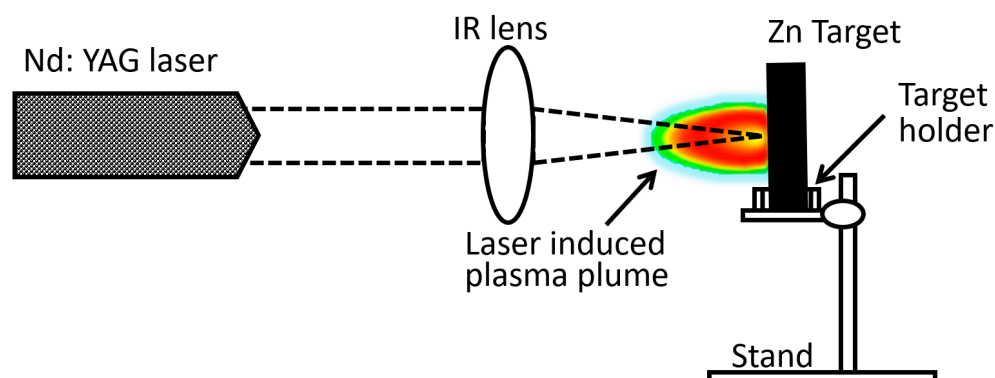


**Figure 1.** A schematic illustration of the experimental setup.

## 2.2. Instrumentation

Advanced instrumental techniques were applied to characterize and examine the material. The surface examination is performed using JEOL JSM-6480LV Scanning Electron Microscope (SEM) with a high resolution (3.0 nm) and magnification ( $18\times$ – $300,000\times$ ) under operating voltage of 0.3 kV–30 kV. Veeco di Innova Atomic Force Microscope (AFM) is used to determine the surface topography. The structural changes are identified using PANalytical X'pert PRO X-ray Diffractometer (XRD) with Cu- $\alpha$  radiation source ( $\lambda = 1.54 \text{ \AA}$ ). The intensity and voltage applied 40–55 mA and 45–60 kV, respectively. The electrical conductivity is measured using four equally spaced probes (2.8 mm spacing) equipped with a current source (Model 6220, Keithley Instruments, Cleveland, OH, USA) ranges between 2–105 mA and voltage source (Model 2182, Keithley, USA) ranges between 1–120 V.

## 3. Results and Discussion

### 3.1. SEM Analysis

The laser allows precise and controlled delivery of an immense amount of energy on a confined area of the target and renders it a highly potent tool for surface modifications. When laser pulses interact with the target surface, their energy is thermalized through electronic and phonon excitations [29]. Consequently, melting occurs that leads to surface modifications in form of regular wavy structures, ripples, ridges, and irregular removal of material as a result of evaporation and exfoliation, following sputtering mechanisms [30,31]. Laser-induced sputtering and swelling of the surface is dominantly a thermal process [32,33]. The SEM scans of test specimens revealed the surface evolution of irradiated targets (Figure 2). The micrographs (Figure 2a–d) highlighted the formation of laser-induced periodic surface structure (LIPSS). Surface alteration by concentric annular ripple formation is prevalent. The mechanism of the ripple formation is attributed to the interference of the incident beam and scattered and diffracted light from surface irregularities at repetitive laser pulses [34].

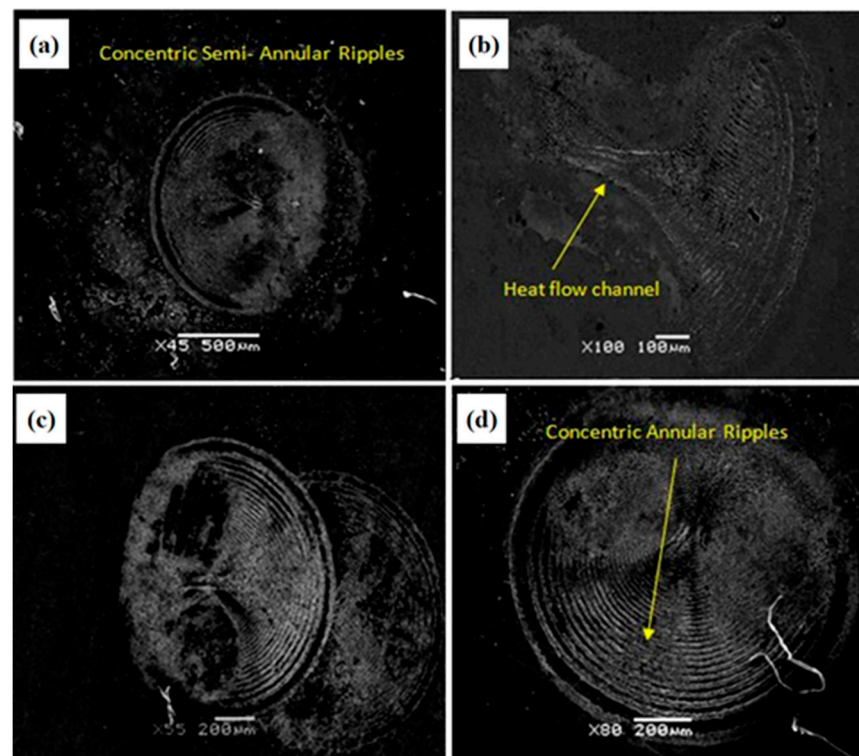


**Figure 2.** SEM micrographs of zinc target surface irradiated by (a) 10, (b) 20, (c) 30, and (d) 40 Nd:YAG laser shots at different magnifications including (a)  $45\times$  (b)  $100\times$  (c)  $200\times$ , and (d)  $200\times$ , respectively.

The scattered light within the irradiated material propagates as a surface wave and interferes with the incident laser light producing intensity patterns over the surface. Another mechanism of the ripple formation is the ejection and redeposition of droplets on the molten surface during the same pulse duration. The mechanical waves induced by this process may freeze on the surface and direct the formation of periodic patterns [34–36]. These structures prevalently depend on the laser parameters such as wavelength, angle of incidence, fluence, and polarization [26,37].

The SEM analysis clearly identify the hydrodynamic sputtering (Figure 3). Figure 3b reveals the melting of surface into the liquid phase, which splashed superficially in response to recoil pressure exerted onto the surface. A material ejection in form of micron-sized spherical globules is also self-evident. The detachment of these globules from the melt pool is caused by high recoil pressure of plasma plume exerted on the target surface [32,38]. Transient melting and re-solidification of the material occurred. Droplets of the material are formed and expelled from the target.

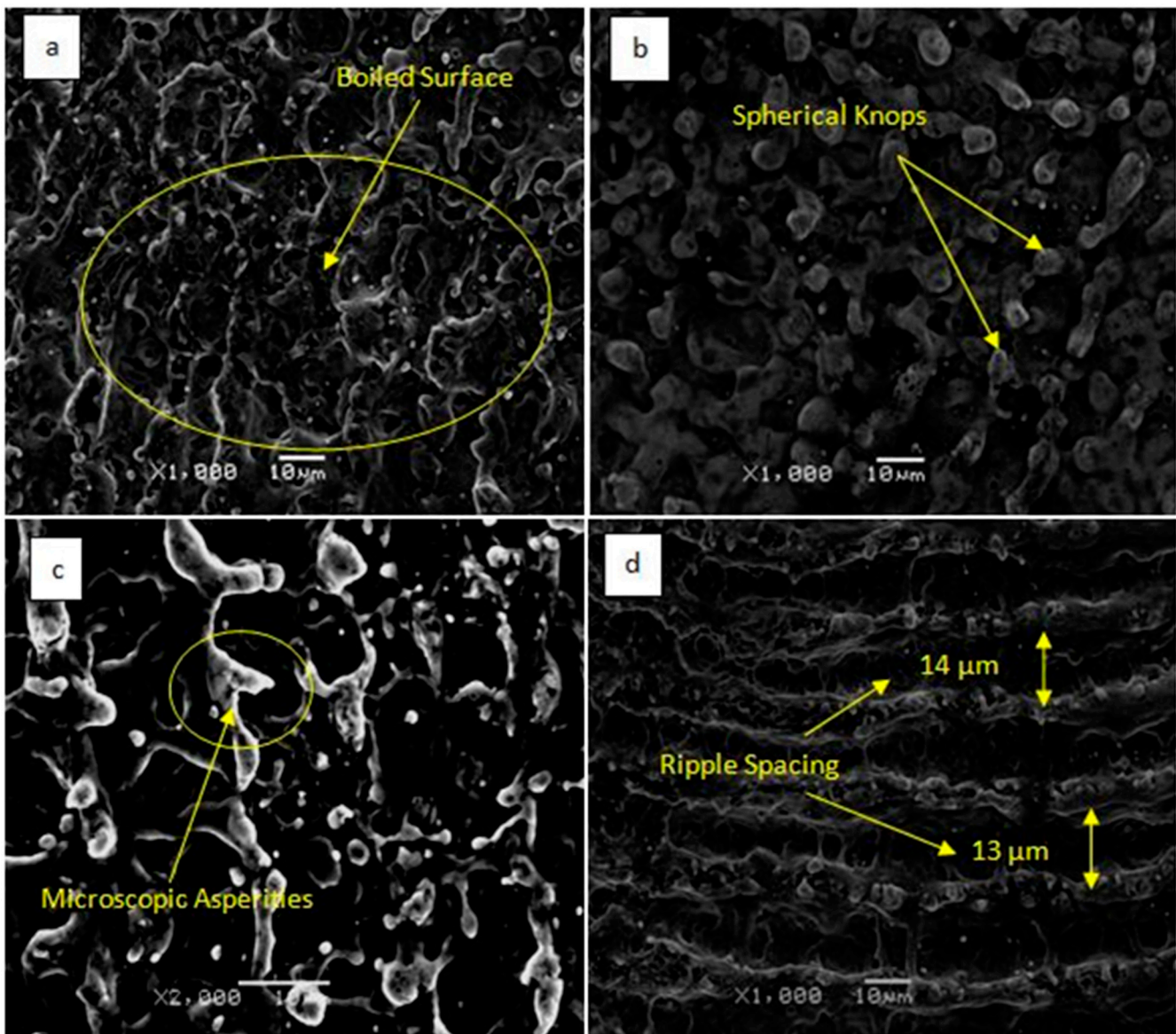


**Figure 3.** SEM micrographs of the zinc target surface irradiated by (a) 10, (b) 20, (c) 30, and (d) 40 Nd:YAG laser shots at higher magnifications including (a) 1000 $\times$ , (b) 1000 $\times$ , (c) 2000 $\times$ , and (d) 1000 $\times$ , respectively.

The surface boiling and bubble bursting can be identified in Figure 3a,b. Small objects with spherical ends, called spherical knobs are formed [35]. It comes out as the surface boiled off because of energy accumulation on the surface and the material is re-solidified before ejection from the target surface. Figure 3c highlights the flow of microscopic asperities in the molten form on the surface. Furthermore, the hydrodynamic sputtering mechanism favors the flow of heat in the lateral dimensions within the molten phase of the material [34,39]. Furthermore, the splashing of material in the form of micron globules takes place owing to the high recoil pressure on the surface. The evolution of the target surface with the formation of low spatial frequency LIPPS (LSFL, or big ripples) can be identified in Figure 3d. The formation of the periodic grooves is based on the modulation of laser incident energy on the target surface caused by the interference of the scattered beam with a refracted beam. Whereas the scattered fields are due to surface roughness and inhomogeneities on the surface [40,41]. To investigate and identify the reliance of ripple spacing on the laser shots, a graph is plotted between ripple spacing and laser shots (Figure 4). A perusal analysis of the graph deduces that the spacing between adjoining ripples is dependent on laser shots.

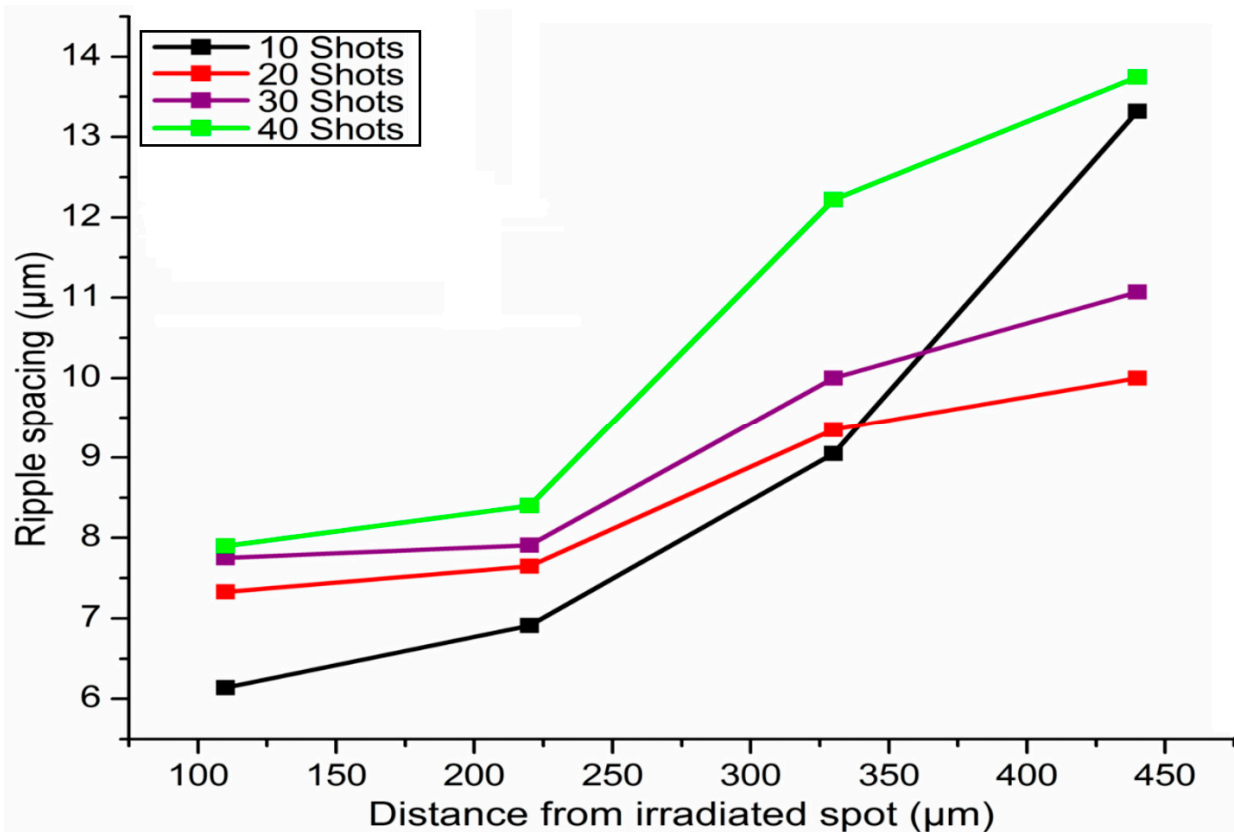


**Figure 4.** Ripple spacing versus distance from the irradiated spot for different Nd: YAG laser shots (10, 20, 30, 40).

### 3.2. AFM Analysis

The AFM micrographs of unexposed and exposed metallic Zinc target surfaces are presented in Figure 5a–d. When the specimens are exposed to multiple Nd: YAG laser shots, ripples are formed and the material surface is swelled due to the transfer of laser energy into heat [42]. The temperature of the workpiece sacrificial layer rises to elevated temperatures and heat energy is promptly quenched in the cold atmospheric bath. Thereby, the surface is crumpled into self-organized periodic grooves due to thermal gradients produced on the surface by incident and scattered laser light fields.

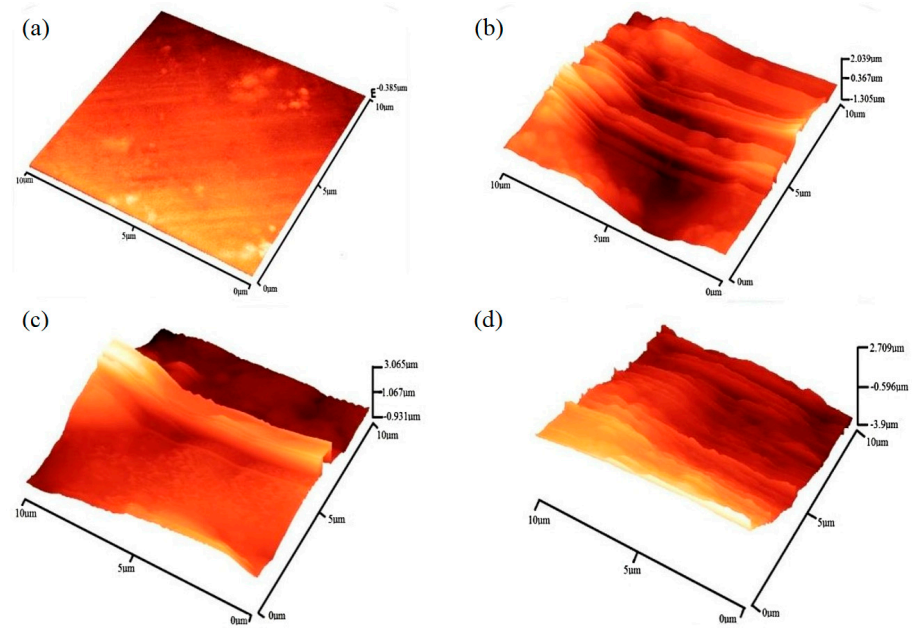


**Figure 5.** AFM images of virgin (a) and irradiated zinc targets by 10 (b), 20 (c), and 30 lasers shots (d).

The mean arithmetic roughness  $R_a$  for the virgin specimen is recorded as  $0.023 \mu\text{m}$ . An average surface roughness is found  $0.469$ ,  $0.932$ ,  $0.230$ , and  $0.160 \mu\text{m}$  in case of 10, 20, 30, and 40 laser shots, respectively. In comparison with virgin samples, about 20 times higher roughness is observed for the samples exposed to 10 shots irradiation. Similarly, exposure to 20 laser shots caused 40 times higher roughness. In case of 30 and 40 laser shots irradiation, growth in average surface roughness values kept continue; however, the fractional step-up in average surface roughness is reduced to 10 to 7 times of its stander value. This variation of average surface roughness with laser shots is explained in Figure 6. It is clear from Figure 6 that the average roughness increased with 20 laser shots because an irradiation produced defects and microstructures like ridges, dips, knops, and micron droplets [43,44]. For higher laser shots (30 to 40), the onset multiple reflection and absorption occurred dominantly and the average surface roughness dropped because of the surface smoothening in a backlash to laser annealing [45,46].

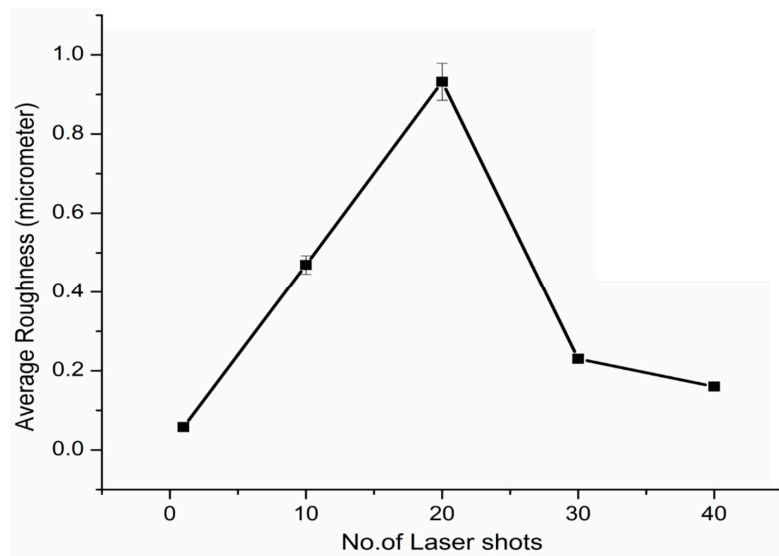


**Figure 6.** A plot of average roughness versus laser shots.

### 3.3. XRD Analysis

Figure 7 shows the XRD patterns of unexposed and exposed Zinc targets. The variation in grain size ( $D$ ), inter-planner spacing ( $d$ ), dislocation line density ( $\delta$ ), and micro-strain ( $\epsilon$ ) for unirradiated and irradiated Zinc targets are determined using Equations (1)–(4) [47,48].

$$D = \frac{K\lambda}{\beta \cos\theta} \tag{1}$$

$$d = \frac{\lambda}{2\sin\theta} \tag{2}$$

$$\delta = \frac{1}{D^2} \tag{3}$$

$$\epsilon = \frac{\beta \cos\theta}{4} \tag{4}$$

here,  $\theta$  is Bragg's angle, constant  $k$  is the shape factor  $\approx 0.94$ ,  $\lambda$  is the wavelength of the X-rays, and  $\beta$  is the full width at half maximum (FWHM) for diffraction peaks. By deeming the entire diffracted X-rays intensity pattern, it comes into prominence that the diffracted intensity is maximum for the plane (101), henceforth this plane is selected for comparison of irradiated and un-irradiated samples.

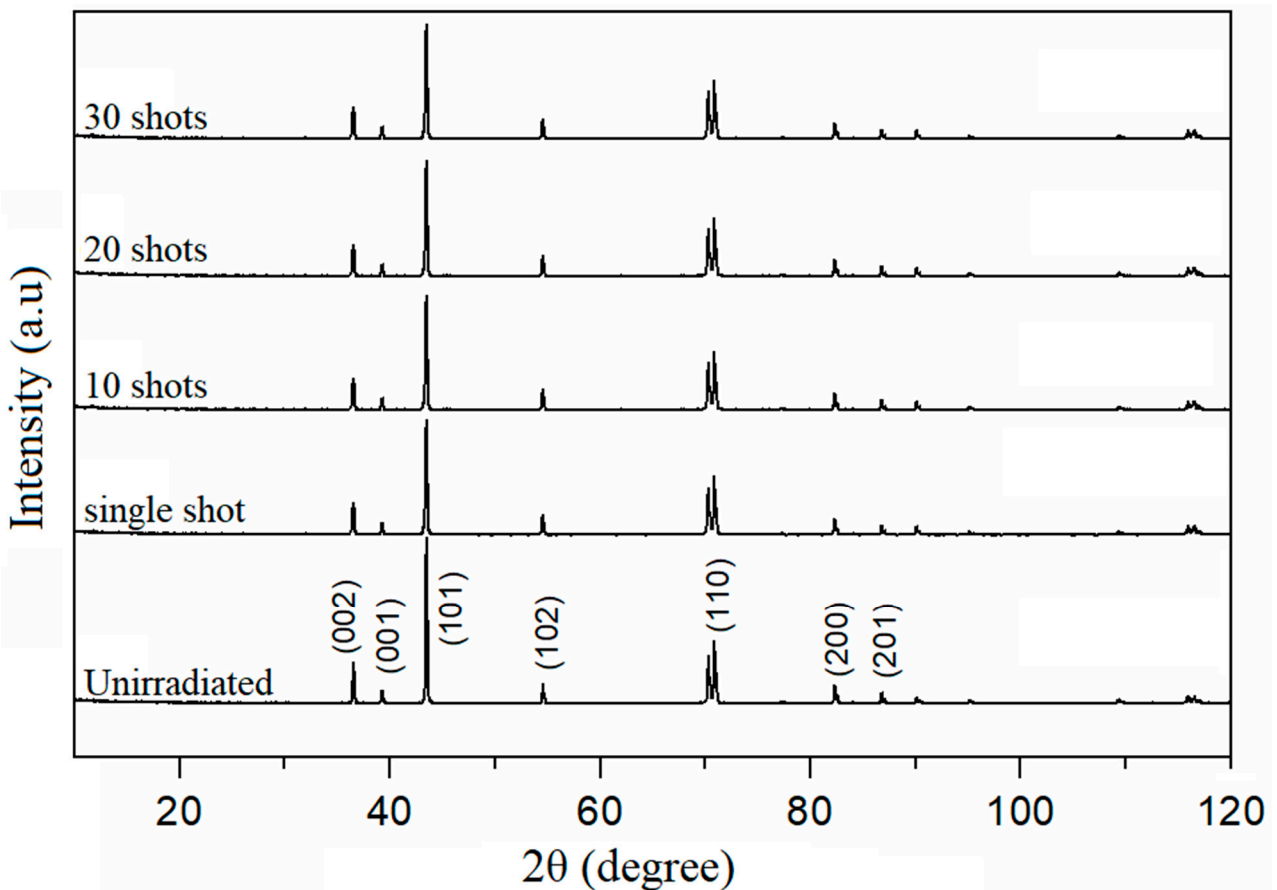


**Figure 7.** The XRD pattern of unirradiated and irradiated Zn target at different shots.

The intensity of the exposed sample falls at angle  $36.297^\circ$  and rises at angles  $38.993^\circ$ ,  $54.337^\circ$ , and  $70.058^\circ$ , but stays constant at  $43.233^\circ$ . This variation in intensity is on account of diffraction and scattering of the incident radiation. The intensity variation of diffracted X-rays vs. Bragg's angle for zinc metal at 20 laser shots is pretty much evident in the plotted curve. This graph unfolds that the intensity of exposed material de-escalates at

angles  $36.297^\circ$ ,  $38.993^\circ$ ,  $54.337^\circ$ , and  $70.058^\circ$ , and remains unchanged at angle  $43.233^\circ$  after irradiation. The intensity of diffracted rays is enhanced due to the re-solidification of molten material as a consequence of atomic diffusion across the grain boundaries and diminishes due to the expansion of the material. Likewise, is the intensity of diffracted X-rays with respect to Bragg's angle for exposed zinc metal for 30 laser shots. The intensity of the exposed sample abates at angles  $36.297^\circ$ ,  $38.993^\circ$ , and  $54.337^\circ$  and accrues at angle  $70.058^\circ$ , but remains stable at  $43.233^\circ$  after irradiation. This variation in intensity is due to non-uniform strains imposed by laser irradiation on the sample surface [39,49].

The statistical information in Figure 8a reveals the relationship between grain size and the number of laser shots. A substantial fall in grain size is observed with a rise in the number of laser shots. About  $0.057 \mu\text{m}$  grain size is determined for 40 laser shots. The trend in Figure 8b gives evidence of the variation in dislocation line density with the number of laser shots. A gradual rise in dislocation line density is observed with an increase in number of laser shots. Figure 8c shows the variation in micro-strain with a rise in laser shots. A steady escalation is noticed in micro-strain for 20 laser shots. A slight fall in value for the next 10 laser shots corresponds to the semi-annealing effect, followed by a dramatic rise in micro-strain at 40 laser shots.

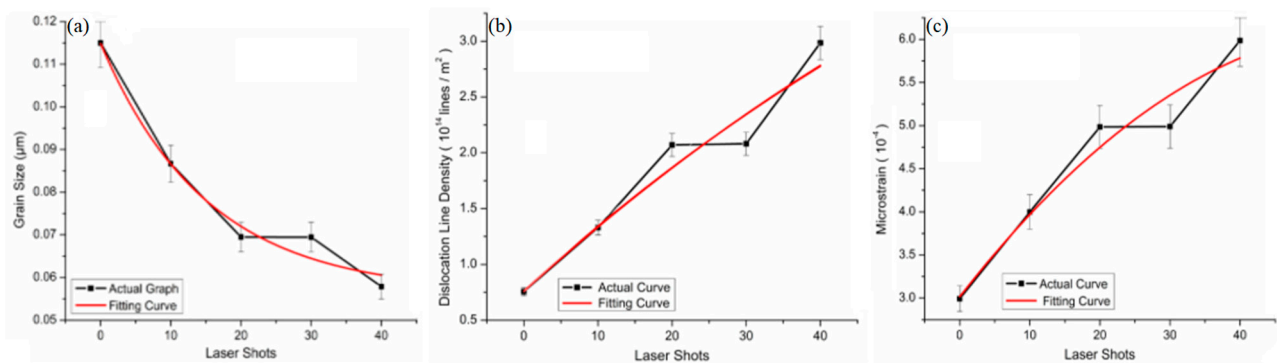


**Figure 8.** The statistical analysis of effect of laser shots on (a) grain size, (b) dislocation line density, and (c) micro-strain.

### 3.4. Electrical Properties

Laser exposure has substantive effects on the electrical properties of metals. Laser irradiation disturbs the lattice arrangement through defect generation. Consequently, these defects accouter nucleation sites for dislocations and invoke to decrease the conductivity of metals. In the proximity of interaction, energetic electrons are generated by the laser radiations, and multiple defects e.g., point, line, and volume are produced. Unexposed zinc samples cannot be deemed 100% defect-free as since lattice vibrations constitute one form of imperfection [50,51]. Regardless of laser-induced damages, the crystallite size defines the conductivity effectively. Small crystallite size concludes for larger scattering probability for the electrons impelling across crystallite boundaries [52]. Additionally, the electrical properties of laser-treated targets vary with the extent of the laser-induced damages depending upon the laser properties such as its wavelength and energy. In our case, with the increase in laser pulses, a decrease in electrical conductivity is more pronounced and meaningful, which may be due to the enhanced photophysical and photochemical processes. These enhanced processes are accountable for the generation of more structural defects, dislocations, and imperfections such as frenkel pair, interstices, crevices, cracks, and voids. Adding more to this, photon-phonon interaction can also directly cause the lattice displacement from original positions [53,54].

Electrical conductivity is being defined as the electric current density per unit applied electric field. We determined the electrical conductivity of virgin and laser-treated test specimens using an arrangement of four evenly spaced probes of spacing 2.8 mm placed at the center of the specimen, parallel to its length (2 cm) and precisely located at the center of

the test specimen (1 cm). Electric current ( $I$ ) is allowed to flow through the outer two probes (Keithley: Model 6220DC Current Source: Range: 2–105 mA) and corresponding potential difference ( $\Delta V$ ) was measured across the inner two probes (Keithley 2182A Nanovoltmeter: Range: 1 nV to 120 V). Electrical conductivity  $\sigma$  ( $\text{ohm m}^{-1}$ ) is determined by Equation (5).

$$\sigma = \frac{\ln 2}{\pi h} \left( \frac{I}{\Delta V} \right) \quad (5)$$

here,  $h$  is the thickness of the specimen (0.1 cm). An exponential trend is found in the reduction of electrical conductivity of zinc metal with laser shots as shown in Figure 9. Equation (6) is used for linear curve fitting of conductivity.

$$y = A_1 \exp(-x/t_1) + y_0 \quad (6)$$

here,  $x$  and  $y$  show the number of laser shots and electrical conductivity, respectively.  $y_0 = 8.53 \times 10^7$ ,  $A_1 = 9.37 \times 10^7$ , and  $t_1 = 14.22$ . The correlation factor is determined 0.97.

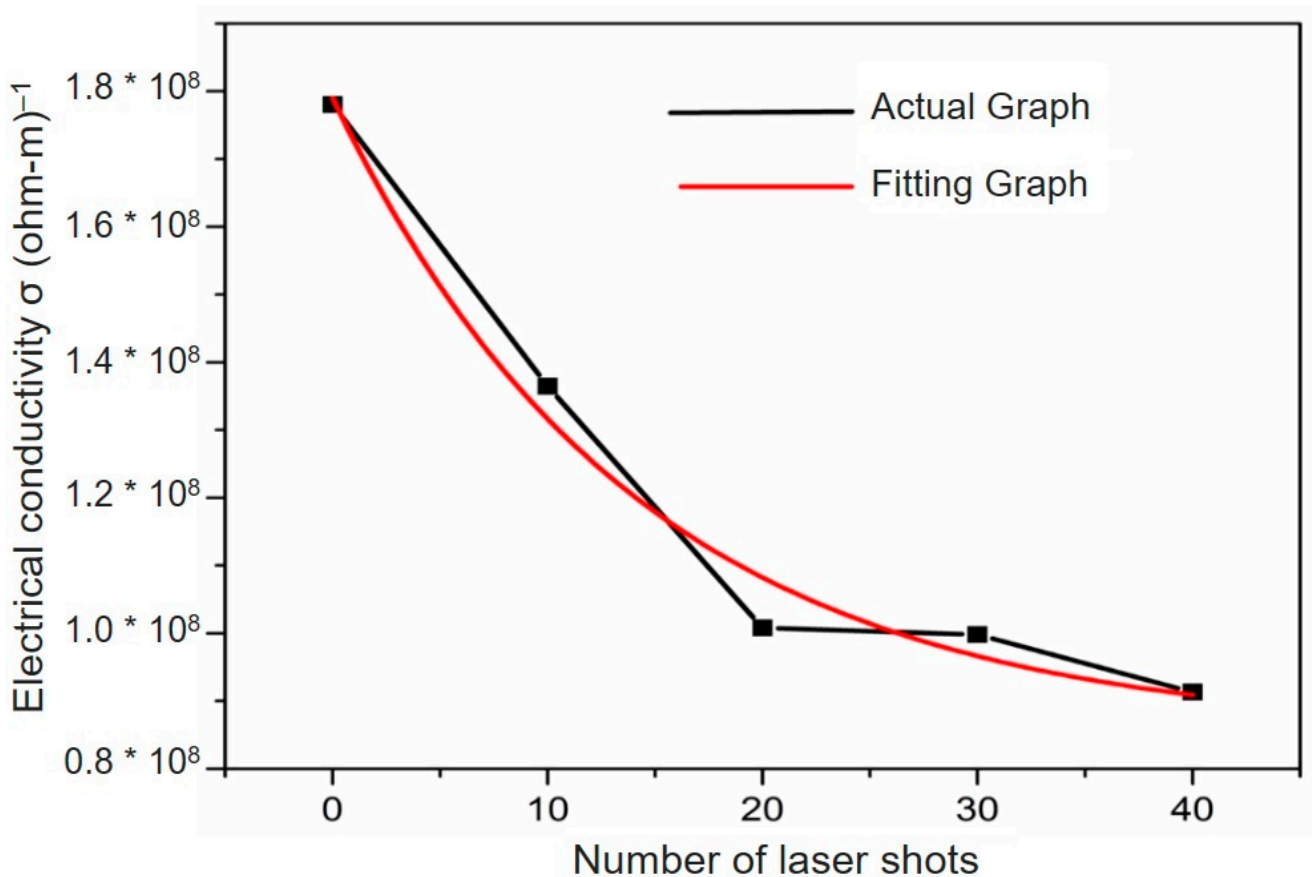


**Figure 9.** A plot of laser shots vs. electrical conductivity.

In conclusion, the irradiation of the Zinc targets caused morphological changes such as ripple structures and topographical surface alteration as observed in SEM and AFM analysis. The XRD analysis did not indicate significant structural change in the crystal structure; however, an exponential descending trend in electrical conductivity is observed with an increase in number of laser shots.

#### 4. Conclusions

Metallic Zinc targets were investigated for morphological, topographical, structural, and electrical properties changes after irradiation with nanosecond Nd: YAG laser pulses. Concentric annular ripples structures formation is found to be a dominant phenomenon

accompanied by hydrodynamical and thermal sputtering. The periodicity of the laser-induced periodic surface structure (LIPPS) springs up to be highly dependent on the laser shots. Surface defects formation and roughness alteration observed. The stresses induced by IR radiation are incapable to produce physical structural changes. The electrical conductivity of the laser shined targets declined exponentially with the increase in laser shots.

**Author Contributions:** Conceptualization, M.A. and A.L.; methodology, M.A. and M.S.R.; software, A.A. and S.A.K.; validation, S.A.K. and A.H.; formal analysis, A.A.; writing—original draft preparation, M.A. and M.K.S.; writing—review and editing, M.K.S.; supervision, A.L. and M.K.S. Funding Acquisition, M.K.S. All authors have read and agreed to the published version of the manuscript.

**Funding:** This research received no external funding.

**Data Availability Statement:** Not applicable.

**Acknowledgments:** We are thankful to the “Center for Advanced Studies in Physics” (CASP) Government College University, Lahore, Pakistan, for providing us the SEM facility to characterize the irradiated specimens.

**Conflicts of Interest:** The authors declare no conflict of interest.

## References

1. Khan, A.A.; Shahid, M.K. Identification of radiation processing of different plant foods of Pakistan origin using the rapid technique of Electron Spin Resonance (ESR) spectrometry. *Radiat. Phys. Chem.* **2022**, *204*, 110667. [[CrossRef](#)]
2. Mahmoodi, N.M. Surface modification of magnetic nanoparticle and dye removal from ternary systems. *J. Ind. Eng. Chem.* **2015**, *27*, 251–259. [[CrossRef](#)]
3. Kondratenko, V.S.; Saprykin, D.L.; Tretiyakova, O.N.; Tuzhilin, D.N. Investigation of Laser Technology for Cutting Mica. *Glas. Ceram.* **2022**, *78*, 486–489. [[CrossRef](#)]
4. Mahmoodi, N.M.; Arami, M. Numerical finite volume modeling of dye decolorization using immobilized titania nanophotocatalysis. *Chem. Eng. J.* **2009**, *146*, 189–193. [[CrossRef](#)]
5. Asif, M.; Latif, A.; Ali, A.; Fuwad, A.; Rafique, M.S.; Nawaz, M.H.; Shahid, M.K. High energy ion irradiation effect on electrical and optical properties of polymers. *Radiat. Phys. Chem.* **2022**, *192*, 109931. [[CrossRef](#)]
6. Gonçalves, L.F.F.F.; Duarte, F.M.; Martins, C.I.; Paiva, M.C. Laser welding of thermoplastics: An overview on lasers, materials, processes and quality. *Infrared Phys. Technol.* **2021**, *119*, 103931. [[CrossRef](#)]
7. Nguyen, A.T.; Phung, V.D.; Mittova, V.O.; Ngo, H.D.; Vo, T.N.; Le Thi, M.L.; Nguyen, V.H.; Mittova, I.Y.; Le, M.L.P.; Ahn, Y.N.; et al. Fabricating nanostructured HoFeO<sub>3</sub> perovskite for lithium-ion battery anodes via co-precipitation. *Scr. Mater.* **2022**, *207*, 114259. [[CrossRef](#)]
8. Anwer, G.; Acherjee, B. Laser polymer welding process: Fundamentals and advancements. *Mater. Today Proc.* **2022**, *61*, 34–42. [[CrossRef](#)]
9. Ghosh, A.; Biswas, S.; Turner, T.; Kietzig, A.-M.; Brochu, M. Surface, microstructure, and tensile deformation characterization of LPBF SS316L microstruts micromachined with femtosecond laser. *Mater. Des.* **2021**, *210*, 110045. [[CrossRef](#)]
10. Gao, J.; Wu, Y.; Zhang, Z.; Zhao, D.; Zhu, H.; Xu, K.; Liu, Y. Achieving amorphous micro-nano superhydrophobic structures on quartz glass with a PTFE coating by laser back ablation. *Opt. Laser Technol.* **2022**, *149*, 107927. [[CrossRef](#)]
11. Liu, S.; Chew, Y.; Weng, F.; Sui, S.; Du, Z.; Man, Y.; Ng, F.L.; Bi, G. Effects of laser pulse modulation on intermetallic compounds formation for welding of Ti-6Al-4V and AA7075 using AA4047 filler. *Mater. Des.* **2022**, *213*, 110325. [[CrossRef](#)]
12. Zhang, J.; Yuan, W.; Song, B.; Yin, S.; Wang, X.; Wei, Q.; Shi, Y. Towards understanding metallurgical defect formation of selective laser melted wrought aluminum alloys. *Adv. Powder Mater.* **2022**, *1*, 100035. [[CrossRef](#)]
13. Wen, Q.; Chen, J.; Wei, X.; Lu, J.; Huang, H.; Cui, C.; Jiang, F. Crystal orientation-dependent scribing of A-, C-, and M-plane sapphires by an ultraviolet laser. *Ceram. Int.* **2022**, *48*, 18842–18854. [[CrossRef](#)]
14. Li, X.; Feng, W.; Zhang, X.; Lin, S.; Chen, Y.; Chen, C.; Chen, S.; Wang, W.; Zhang, Y. Facile fabrication of laser-scribed-graphene humidity sensors by a commercial DVD drive. *Sens. Actuators B Chem.* **2020**, *321*, 128483. [[CrossRef](#)]
15. Ismail, A.M.; Nasrallah, D.A.; El-Metwally, E.G. Modulation of the optoelectronic properties of polyimide (Kapton-H) films by gamma irradiation for laser attenuation and flexible space structures. *Radiat. Phys. Chem.* **2022**, *194*, 110026. [[CrossRef](#)]
16. Farooq, A.; Alquaity, A.B.S.; Raza, M.; Nasir, E.F.; Yao, S.; Ren, W. Laser sensors for energy systems and process industries: Perspectives and directions. *Prog. Energy Combust. Sci.* **2022**, *91*, 100997. [[CrossRef](#)]
17. Mostafa, A.M. The enhancement of nonlinear absorption of Zn/ZnO thin film by creation oxygen vacancies via infrared laser irradiation and coating with Ag thin film via pulsed laser deposition. *J. Mol. Struct.* **2021**, *1226*, 129407. [[CrossRef](#)]
18. Madiba, I.G.; Khanyile, B.S.; Mabakachaba, B.; Mbambo, M.C.; Bashir, A.K.H.; Ezema, F.; Maaaza, M. Cluster-coalesced defects induced by gamma irradiation on pulsed laser deposited VO<sub>2</sub> thin films. *Mater. Today Proc.* **2022**, *53*, 429–431. [[CrossRef](#)]

19. Barmina, E.V.; Stratakis, E.; Barberoglou, M.; Stolyarov, V.N.; Stolyarov, I.N.; Fotakis, C.; Shafeev, G.A. Laser-assisted nanostructuring of Tungsten in liquid environment. *Appl. Surf. Sci.* **2012**, *258*, 5898–5902. [[CrossRef](#)]
20. Qian, Q.; Wang, Q.; Qian, H. Effect of different energy loading forms on laser irradiation of metal target. *IOP Conf. Ser. Earth Environ. Sci.* **2019**, *300*, 42095. [[CrossRef](#)]
21. Sakurai, H.; Konishi, K.; Tamaru, H.; Yumoto, J.; Kuwata-Gonokami, M. Direct correlation of local fluence to single-pulse ultrashort laser ablated morphology. *Commun. Mater.* **2021**, *2*, 38. [[CrossRef](#)]
22. Lowndes, D.H.; Fowlkes, J.D.; Pedraza, A.J. Early stages of pulsed-laser growth of silicon microcolumns and microcones in air and SF<sub>6</sub>. *Appl. Surf. Sci.* **2000**, *154–155*, 647–658. [[CrossRef](#)]
23. Chen, L.; Chen, Z.; Shimada, K.; Mizutani, M.; Kuriyagawa, T. Electric field analysis coupled with the two-temperature model to elucidate the generation process of laser-induced periodic surface structure. *J. Mater. Process. Technol.* **2022**, *305*, 117601. [[CrossRef](#)]
24. Li, Z.; Wu, Q.; Jiang, X.; Zhou, X.; Liu, Y.; Hu, X.; Zhang, J.; Yao, J.; Xu, J. Formation mechanism of high spatial frequency laser-induced periodic surface structures and experimental support. *Appl. Surf. Sci.* **2022**, *580*, 152107. [[CrossRef](#)]
25. Djouder, M.; Itina, T.E.; Deghiche, D.; Lamrous, O. Modelling the formation of nanostructures on metal surface induced by femtosecond laser ablation. *Appl. Surf. Sci.* **2012**, *258*, 2580–2583. [[CrossRef](#)]
26. Latif, A.; Anwar, M.S.; Aleem, M.A.; Rafique, M.S.; Khaleeq-Ur-Rahman, M. Influence of number of laser shots on laser induced microstructures on Ag and Cu targets. *Laser Part. Beams* **2009**, *27*, 129–136. [[CrossRef](#)]
27. Moezzi, A.; McDonagh, A.M.; Cortie, M.B. Zinc oxide particles: Synthesis, properties and applications. *Chem. Eng. J.* **2012**, *185–186*, 1–22. [[CrossRef](#)]
28. Mahmoodi, N.M.; Bashiri, M.; Moeen, S.J. Synthesis of nickel–zinc ferrite magnetic nanoparticle and dye degradation using photocatalytic ozonation. *Mater. Res. Bull.* **2012**, *47*, 4403–4408. [[CrossRef](#)]
29. Li, X.; Guan, Y. Theoretical fundamentals of short pulse laser–metal interaction: A review. *Nanotechnol. Precis. Eng.* **2020**, *3*, 105–125. [[CrossRef](#)]
30. Latif, A.; Rafiq, M.S.; Bhatti, K.A.; Mahmood, N. Surface and structural investigations on laser irradiated P-type silicon. *Radiat. Eff. Defects Solids* **2014**, *169*, 506–512. [[CrossRef](#)]
31. Bereznai, M.; Pelsöczy, I.; Tóth, Z.; Turzó, K.; Radnai, M.; Bor, Z.; Fazekas, A. Surface modifications induced by ns and sub-ps excimer laser pulses on titanium implant material. *Biomaterials* **2003**, *24*, 4197–4203. [[CrossRef](#)] [[PubMed](#)]
32. Latif, A.; Khaleeq-ur-Rahman, M.; Bhatti, K.A.; Rafique, M.S.; Hayat, A. Microstructural Morphological Changes in LaserIrradiated Platinum. *J. Mod. Phys.* **2011**, *2*, 875–884. [[CrossRef](#)]
33. Miller, J.C.; Haglund, R.F. *Laser Ablation and Desorption*; Academic Press: San Diego, CA, USA, 1998; Volume 30.
34. Khaleeq-ur-Rahman, M.; Siraj, K.; Rafique, M.S.; Bhatti, K.A.; Latif, A.; Jamil, H.; Basit, M. Laser induced plasma plume imaging and surface morphology of silicon. *Nucl. Instrum. Methods Phys. Res. Sect. B Beam Interact. Mater. Atoms* **2009**, *267*, 1085–1088. [[CrossRef](#)]
35. Vincenc Obona, J.; Ocelík, V.; Skolski, J.Z.P.; Mitko, V.S.; Römer, G.R.B.E.; Huis in't Veld, A.J.; De Hosson, J.T.M. On the surface topography of ultrashort laser pulse treated steel surfaces. *Appl. Surf. Sci.* **2011**, *258*, 1555–1560. [[CrossRef](#)]
36. Behera, R.R.; Sankar, M.R.; Baruah, P.K.; Sharma, A.K.; Khare, A. Experimental investigations of nanosecond-pulsed Nd: YAG laser beam micromachining on 304 stainless steel. *J. Micromanuf.* **2018**, *1*, 62–75. [[CrossRef](#)]
37. Gaspar, G.; Rodrigues, J.; Fernandes, A.J.S.; Soares, M.R.; Monteiro, T.; Silva, R.F.; Costa, F.M. Nd: YAG laser scribed zinc oxide on semi-flexible copper foils. *Mater. Lett. X* **2020**, *5*, 100038. [[CrossRef](#)]
38. Helali, M.Y.; Saadeldin, M.M.; Ibrahim, M. Effects of laser irradiation on the microstructure and surface morphology of zinc oxide doped with different additives. *Curr. Sci.* **2019**, *116*, 1818. [[CrossRef](#)]
39. Naeem, S.; Mehmood, T.; Wu, K.M.; Khan, B.S.; Majid, A.; Siraj, K.; Mukhtar, A.; Saeed, A.; Riaz, S. Laser Surface Hardening of Gun Metal Alloys. *Materials* **2019**, *12*, 2632. [[CrossRef](#)]
40. Angelsky, O.V.; Maksimyak, P.P. Optical Correlation Diagnostics of Surface Roughness. In *Handbook of Coherent Domain Optical Methods*; Tuchin, V.V., Ed.; Springer: New York, NY, USA, 2019; pp. 43–92. ISBN 978-0-387-29989-1.
41. Germer, T.A.; Sharma, K.A.; Brown, T.G.; Oliver, J.B. Polarized optical scattering by inhomogeneities and surface roughness in an anisotropic thin film. *J. Opt. Soc. Am. A. Opt. Image Sci. Vis.* **2017**, *34*, 1974–1984. [[CrossRef](#)]
42. Savolainen, J.-M.; Christensen, M.S.; Balling, P. Material swelling as the first step in the ablation of metals by ultrashort laser pulses. *Phys. Rev. B* **2011**, *84*, 193410. [[CrossRef](#)]
43. Vilar, R. Microstructure Modification: Generation of Crystal Defects and Phase Transformations. In *Handbook of Laser Micro- and Nano-Engineering*; Sugioka, K., Ed.; Springer International Publishing: Cham, Switzerland, 2020; pp. 1–60. ISBN 978-3-319-69537-2.
44. Robertson, S.M.; Kaplan, A.F.H.; Frostevarg, J. Material ejection attempts during laser keyhole welding. *J. Manuf. Process.* **2021**, *67*, 91–100. [[CrossRef](#)]
45. Sala, F.; Paíé, P.; Martínez Vázquez, R.; Osellame, R.; Bragheri, F. Effects of Thermal Annealing on Femtosecond Laser Micromachined Glass Surfaces. *Micromachines* **2021**, *12*, 180. [[CrossRef](#)] [[PubMed](#)]
46. Carlomagno, I.; Lucarini, I.; Secchi, V.; Maita, F.; Polese, D.; Mirabella, S.; Franzò, G.; Notargiacomo, A.; Di Santo, G.; Gonzalez, S.; et al. Surface Zn enrichment induced by excimer laser annealing in ZnO nanorods. *Appl. Surf. Sci.* **2022**, *587*, 152313. [[CrossRef](#)]

47. Thomas, K.; Parol, V.; Karuppasamy, P.; Pandian, M.S.; Ramsamy, P.; Prabhu, A.N. Influence of  $^{60}\text{Co}$  gamma irradiation on the structural and optical properties of 2-aminopyridinium 4-nitrophenolate 4-nitrophenol crystals. *Curr. Appl. Phys.* **2022**, *37*, 1–7. [[CrossRef](#)]
48. Shahid, M.K.; Kim, Y.; Choi, Y.-G. Magnetite synthesis using iron oxide waste and its application for phosphate adsorption with column and batch reactors. *Chem. Eng. Res. Des.* **2019**, *148*, 169–179. [[CrossRef](#)]
49. Bai, Y.; Zeng, J.; Huang, J.; Cheng, Z.; Zhao, Q.; Liang, D. Non-uniform strain field reconstruction of FBG using an adaptive Nelder–Mead algorithm. *Opt. Commun.* **2021**, *484*, 126689. [[CrossRef](#)]
50. Butt, M.Z.; Ali, D.; Tanveer, M.U.; Naseem, S. Surface roughness and electrical resistivity of high-purity zinc irradiated with nanosecond visible laser pulses. *Appl. Surf. Sci.* **2014**, *305*, 466–473. [[CrossRef](#)]
51. Itakura, T.; Matsui, H.; Tada, T.; Kitagawa, S.; Demessence, A.; Horike, S. The role of lattice vibration in the terahertz region for proton conduction in 2D metal-Organic frameworks. *Chem. Sci.* **2020**, *11*, 1538–1541. [[CrossRef](#)]
52. Butt, M.Z.; Ali, D.; Bashir, F.; Ishtiaq, M. Effects of IR Laser Shots on the Surface Hardness and Electrical Resistivity of High-Purity Iron. *J. Mater. Eng. Perform.* **2014**, *23*, 772–779. [[CrossRef](#)]
53. Jiang, H.; Yan, X.; Liang, H.; Luo, R.; Chen, X.; Chen, Y.; Lin, Q. High harmonic optomechanical oscillations in the lithium niobate photonic crystal nanocavity. *Appl. Phys. Lett.* **2020**, *117*, 81102. [[CrossRef](#)]
54. Esposito, M.; Titimbo, K.; Zimmermann, K.; Giusti, F.; Randi, F.; Boschetto, D.; Parmigiani, F.; Floreanini, R.; Benatti, F.; Fausti, D. Photon number statistics uncover the fluctuations in non-equilibrium lattice dynamics. *Nat. Commun.* **2015**, *6*, 10249. [[CrossRef](#)] [[PubMed](#)]

**Disclaimer/Publisher’s Note:** The statements, opinions and data contained in all publications are solely those of the individual author(s) and contributor(s) and not of MDPI and/or the editor(s). MDPI and/or the editor(s) disclaim responsibility for any injury to people or property resulting from any ideas, methods, instructions or products referred to in the content.